

ATMOSPHERIC COMPENSATION USING A GEOMETRICALLY-COMPENSATED EMPIRICAL LINE METHOD

Stephen R. Lach^{a,b} and John P. Kerekes^b

^a United States Air Force

^b Digital Imaging and Remote Sensing Laboratory, Rochester Institute of Technology
54 Lomb Memorial Drive, Rochester, NY 14623
sf11194@cis.rit.edu, kerekes@cis.rit.edu

DISCLAIMER: THE VIEWS EXPRESSED IN THIS ARTICLE ARE THOSE OF THE AUTHORS AND DO NOT REFLECT THE OFFICIAL POLICY OR POSITION OF THE U.S. AIR FORCE, DEPARTMENT OF DEFENSE, OR U.S. GOVERNMENT.

ABSTRACT

This paper presents a geometric extension to the well known Empirical Line Method (ELM) for atmospheric compensation, enabling improved results through the use of 3D scene geometry. Typically, this geometry is assumed to be known, either through direct measurement or analysis of other imagery such as lidar or photogrammetric products. However, when the scene geometry is unknown and only spectral information is available, in certain cases estimates of the surface orientation may be obtained directly from image brightness values. In this paper we derive a means to determine surface orientation estimates from a pair of brightness images, and then use this geometric information to improve the ELM solution.

Index Terms— atmospheric measurements, hyperspectral, remote sensing

1. INTRODUCTION

Remote sensing provides us with the ability to gain an understanding of the world through various imaging techniques and modalities. This is especially true given the recent advances in hyperspectral sensing systems, where imagers with many spectral channels sample the sensor-bound radiance, providing a continuum of information as a function of wavelength. The underlying premise is that the information of interest is a function of the spectral reflectance function of the objects being observed. Therefore, in order to effectively use hyperspectral imagery, the received images must be either calibrated to reflectances, or the reflectances must be forward-propagated to image-space. This paper will focus on transforming the received radiance (which may be in uncalibrated digital counts) to reflectance values. Specifically, we will present a geometric extension to the popular Empirical Line Method (ELM) of atmospheric compensation, which makes use of

3D scene geometry obtained from lidar imagery or other sources. We also will discuss a method of estimating the orientation information required for this approach directly from the spectral imagery.

2. BACKGROUND

There are many methods of performing atmospheric compensation in the literature. Physics-based approaches such as the Fast Line-of-sight Atmospheric Analysis of Spectral Hypercubes (FLAASH) [1] use radiative transfer models like the Moderate Resolution Atmospheric Transmission (MODTRAN) [2] to estimate and remove atmospheric effects from calibrated data.

However, as noted in [3], if large (approximately 3 times the ground instantaneous field of view), near-Lambertian ground panels of known reflectance are available, one of the most attractive techniques for recovering reflectance curves from the sensed spectral radiance is through the Empirical Line Method (ELM), since the received radiance does not have to be calibrated first for the technique to work. This is the method used for reflectance retrieval in this paper, and it will be described and expanded upon in the following section.

3. APPROACH

To perform the basic ELM per [4], we assume a received radiance model of

$$L_{sensor} = \left(\frac{E_s' \cos \theta \tau_1}{\pi} + F \cdot L_d \right) \tau_2 r + L_u \quad (1)$$

at each wavelength, where E_s' is the direct exo-atmospheric solar irradiance, L_d is the downwelled radiance, F is a shape factor between 0 and 1 used to scale L_d , τ_1 is the sun-target path transmission, τ_2 is the target-sensor path transmission, r

is the target reflectance and L_u is the upwelled radiance. θ is the angle between the target-sun vector and the target's normal vector, and is effectively the angle at which direct solar irradiance is incident upon the target. The atmospheric calibration may then be achieved by noting this model is linear with respect to reflectance,

$$L_{\text{sensor}} = m \cdot r + b, \quad (2)$$

and the slope (m) and intercept (b) may be determined through a regression with known reflectance values for each band. Frequently, these known reflectance values are obtained via ground measurement of reflectance panels, and in most cases, b is assumed to be constant throughout the scene.

3.1. Using Geometric Information to Improve the ELM

When lidar data or other three-dimensional information is available, improved results may be obtained by using proper angular values, θ , and shape factors, F , at each point being considered. In a manner analogous to that presented in [3], we may compensate for object slope effects if the ratio of downwelled radiance to total received radiance at the target is known. This is accomplished by using the original ELM slope and intercept, and applying

$$L_{\text{sensor}} = \left((m - \ell \cdot m) \frac{\cos \theta_t}{\cos \theta_c} + \frac{F_t}{F_c} \cdot \ell \cdot m \right) r + b, \quad (3)$$

where

$$\ell = \frac{L_d}{(E_s \cos \theta_c \pi^{-1} + L_d)}. \quad (4)$$

In these equations, θ_c is the angle between the target-to-sun vector and the normal vectors for the targets of known reflectance, and F_c is the shape factor for the calibration targets.

In practice, ℓ is ideally obtained through a field measurement at the time of the collection. However, if such a measurement is not feasible, this ratio may be estimated either through atmospheric propagation models such as MODTRAN or through in-scene techniques such as that presented in [4]. An alternate method for estimating this ratio is also available if fully-resolved pixels of a Lambertian material are available on two planar faces with known orientations (such as a residential roof structure). In this case, the ratio ℓ may be determined at each wavelength by setting the reflectance values of the two planar faces equal to each other. That is, we establish

$$[(m - \ell m)k_1 + F_1 \ell m][L_2 - L_u] = [(m - \ell m)k_2 + F_2 \ell m][L_1 - L_u] \quad (5)$$

at each wavelength, which yields

$$\ell = \frac{k_1(L_2 - L_u) + k_2(L_u - L_1)}{(k_1 - F_1)(L_2 - L_u) + (k_2 - F_2)(L_u - L_1)}, \quad (6)$$

where

$$k_1 = \frac{\cos \theta_1}{\cos \theta_c}, \quad k_2 = \frac{\cos \theta_2}{\cos \theta_c}, \quad F_1 = \frac{F_{\text{target } 1}}{F_c}, \quad F_2 = \frac{F_{\text{target } 2}}{F_c}. \quad (7)$$

In this development, θ_i is the angle at which the solar irradiance is incident upon the i^{th} facet, and L_i is the received radiance from a pixel on the image of the i^{th} facet. When applying Equations 3 and 6, we have termed the solution the geometrically-compensated empirical line method (GC-ELM).

3.1. Brightness-Derived Orientation Mapping

If the orientations of the two planar faces needed for the GC-ELM are unknown, this geometry may be estimated from image brightness values if multiple images are available and certain constraints are met. This approach is termed Brightness-Derived Orientation Mapping (BDOM), and it is essentially a shape-from-shading approach to estimating a plane's azimuth and elevation angles. Two variations of this approach are presented below. The first assumes that the orientation of one of the surfaces is known, and we solve for the orientation of the second surface. In the second variation, we do not know the absolute orientation of either surface, but we establish a constraint on the relative geometry of the two surfaces.

In order to complete the BDOM derivation, a simplified radiance propagation model is required. Typically, at higher wavelengths (above 1 micron), both the L_d and L_u terms from Equation 1 become negligible compared to the direct solar term. This is illustrated in Fig. 1, where we plot $E'_s \tau_1 \pi^{-1} / (L_d + L_u)$ versus wavelength. The data for this figure was obtained by using the Digital Imaging and Remote Sensing Image Generation (DIRSIG) software [5], a mature first-principles based hyperspectral image simulation tool developed at the Rochester Institute of Technology over the past 20 years.

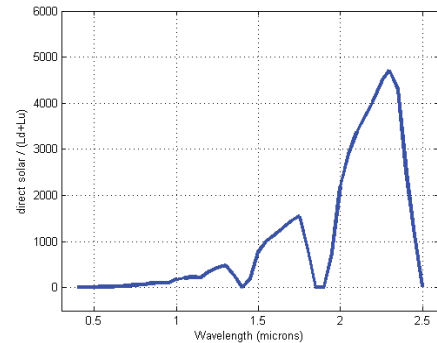


Fig. 1. The ratio of direct solar to downwelled plus upwelled radiances as a function of wavelength

With the contributions of the downwelled and upwelled radiances removed, Equation 1 is simplified to

$$L_{\text{sensor}} = \frac{E_s' \cos \theta_{\tau_1} \tau_2 r}{\pi} = A \cos \theta r \cdot \quad (7)$$

We now need to assume that we have a Lambertian material with reflectance r at two locations a and b , and each location is on a separate planar surface. These locations are imaged at times t_1 and t_2 to provide four brightness values, L_{a1} , L_{a2} , L_{b1} and L_{b2} . Since the reflectance of each point is the same, we are able to write two equations

$$\cos \theta_{ai} = \frac{L_{ai} \cos \theta_{bi}}{L_{bi}}, \quad (8)$$

where i represents either the image at t_1 or t_2 .

For the first BDOM variation, we assume the orientation of one of the planar faces (assume location b) is known (often this surface is assumed to be horizontal). Therefore, if we know the solar geometry at both t_1 and t_2 , we may easily determine θ_{bi} . This information is then used to solve for θ_a at each imaging time, which may subsequently be used to determine two azimuth/elevation angle pairs, each of which is a valid solution to the equations. The actual orientation of the unknown facet will be one of these solutions.

We may conceptualize the geometry as follows. The first image reveals that the normal vector of our unknown surface is a given angular offset ω_1 away from a vector pointing from the unknown facet towards the sun. That is, the potential orientations of the unknown normal vector sweep out a cone of angular width $2\omega_1$ centered on this solar vector. The second image sweeps out a cone of width $2\omega_2$ about the vector pointing to the sun at time t_2 . In general, these two cones intersect along two lines, and these lines define the potential normal vectors for the unknown surface. One line represents the actual orientation of the surface, while the other is an artifact of the ambiguity in the solution. It is fairly easy to see that if three imaging times are used, this ambiguity is effectively removed.

The derivation of the two-image solution is straightforward but lengthy, and the closed form solution is not included here. In practice we have also found that this closed-form solution may lead to ill-conditioned solutions for certain orientations. As such, in many cases we simply cycle through many combinations of azimuth and elevation candidates until the closest equality for Equation 8 is obtained.

For the second BDOM case, we do not require knowledge of either surface's orientation. However, we do assume that the two surfaces have equal elevation angles and opposite azimuths (an offset of π radians). This is the common configuration found on most residential roof

structures. With this constraint, we are able to determine the azimuth and elevation angles of each surface without ambiguity, provided the Lambertian and other previously noted assumptions are met.

In this case, we again assume four instances of Equation 7, one each for brightness values, L_{a1} , L_{a2} , L_{b1} and L_{b2} . Assuming unit length vectors, we may therefore write each equation in the form

$$L_{j,i} = A_i (\vec{s}_i \cdot \vec{n}_{j,i}) r, \quad (9)$$

where \vec{s}_i represents the vector from the target to the sun at time i , and $\vec{n}_{j,i}$ is the unit normal vector for surface location j at time i . A_i is a constant for each time i . These equations may be re-written in terms of the unknown azimuth (α) and elevation (δ) angles according to

$$\begin{aligned} \frac{L_{j,i}}{A_i} &= s_{i1} \cos(\alpha_{j,i}) \sin(\delta_{j,i}) \\ &+ s_{i2} \sin(\alpha_{j,i}) \sin(\delta_{j,i}) + s_{i3} \cos(\delta_{j,i}), \end{aligned} \quad (10)$$

where s_{ik} represents the k^{th} vector component of s at time t_i . Equating the reflectances of the two roof surfaces at a given time yields the equations

$$\begin{aligned} L_{bi} [s_{i1} \cos \alpha_i \sin \delta_i + s_{i2} \sin \alpha_i \sin \delta_i + s_{i3} \cos \delta_i] &= \\ L_{ai} [s_{i1} \cos(\alpha_i + \pi) \sin \delta_i + s_{i2} \sin(\alpha_i + \pi) \sin \delta_i + s_{i3} \cos \delta_i] \end{aligned} \quad (11)$$

Again, the analytical solution of the azimuth and elevation angles from these equations is straightforward but lengthy, and it will not be included here. Also as before, in practice a useable solution may be found by cycling through combinations of azimuth and elevation pairs until an approximate solution is found. We have used Equation 11 to define the quality metric $q=1/\varepsilon$, where

$$\varepsilon = |L_{b1}Q_1 - L_{a1}Q_2| + |L_{b2}Q_3 - L_{a2}Q_4| \quad (12)$$

and

$$\begin{aligned} Q_1 &= s_{11} \cos \alpha \sin \delta + s_{12} \sin \alpha \sin \delta + s_{13} \cos \delta \\ Q_2 &= s_{11} \cos(\alpha + \pi) \sin \delta + s_{12} \sin(\alpha + \pi) \sin \delta + s_{13} \cos \delta \\ Q_3 &= s_{21} \cos \alpha \sin \delta + s_{22} \sin \alpha \sin \delta + s_{23} \cos \delta \\ Q_4 &= s_{21} \cos(\alpha + \pi) \sin \delta + s_{22} \sin(\alpha + \pi) \sin \delta + s_{23} \cos \delta \end{aligned}$$

4. RESULTS

This section shows the results of these techniques as applied to the simulated scene depicted in Fig. 2. This scene was created for use with the DIRSIG image generation tool, and by modeling a hyperspectral imaging sensor, we were able to produce simulated spectral imagery of the virtual location.



Fig. 2. Scene model used for simulated image generation

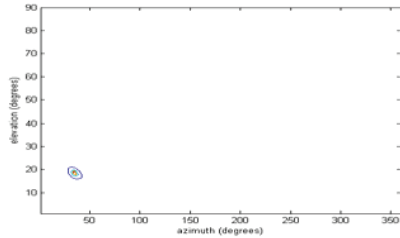


Fig. 3. BDOM result (q-metric) for northern roof pixel

We began by generating two simulated hyperspectral images of this scene, one at 1200h local time and the other at 1600h. Next, we took a single pixel value from the 1.25 micron band (due to the local maxima at that spectral region; reference Fig. 1) from each side of the building roof at each image time to produce four radiance values. These values were then multiplied by a factor of 1.2 to simulate mis-calibration of the sensor-recorded radiance in this band. Cycling through each potential azimuth/elevation pair using the q-metric defined above yielded the result shown in Fig. 3, which estimated the northern roof orientation with an accuracy of better than 2 degrees in both azimuth and elevation.

We next performed a standard ELM for pixels taken from both the north and south roof faces. The result of this compensation is shown in Fig. 4. As expected, the cosine effect causes a difference in calculated reflectance between the two faces. We then used the actual roof orientation angles along with the received radiances to verify the GC-ELM equations, and the result is given in Fig. 5. It is apparent that the computed reflectance values match the truth spectra very well in most bands.

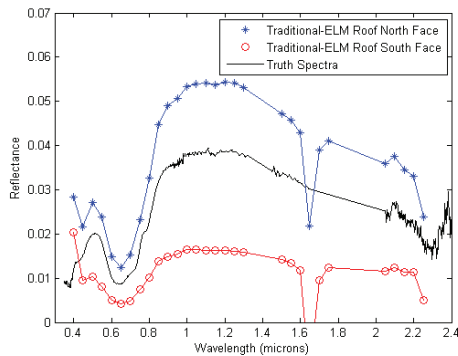


Fig. 4. Standard ELM compensation for north and south roof pixels

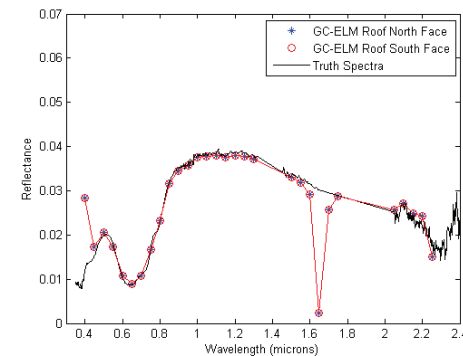


Fig. 5. GC-ELM compensation for north and south roof pixels

5. SUMMARY

In this paper, we presented an extension to the ELM atmospheric compensation algorithm, which enabled improved results through the use of 3D scene geometry. We discussed how knowledge of the scene geometry may help remove the cosine effects of the direct solar radiation if the ratio ℓ were known, and we presented a method to solve for this ratio given certain constraints. Additionally, we discussed techniques for determining the orientation of objects in the scene directly from image brightness values. These orientations could then be used to estimate ℓ , which subsequently improves the ELM solution.

Future work in this area will seek to characterize these algorithms in the presence of noise, as well as to verify the feasibility of the overall approach with real data. A comparison with other in-scene atmospheric compensation approaches is also necessary.

6. REFERENCES

- [1] Adler-Golden, Matthew, Bernstein, Levine, Berk, Richtsmeier, Acharya, Anderson, Felde, Gardner, Hike, Jeong, Pukall, Mello, Ratkowski, and Burke, "Atmospheric correction for shortwave spectral imagery based on MODTRAN4," In Proc. SPIE, Imaging Spectrometry, volume 3753, pp. 61-69, 1999.
- [2] Berk, A., Bernstein, L.S., Anderson, G.P., Acharya, P.K., Robertson, D.C., Chetwynd, J.H., and Adler-Golden, S.M., "MODTRAN cloud and multiple scattering upgrades with application to AVIRIS," *Remote Sens. Environ.*, 65:367-375, 1998.
- [3] Schott, J. *Remote Sensing: The Image Chain Approach, Second Edition*, Oxford University Press, New York, 2007.
- [4] Piech, K. and J. Walker, "Interpretation of Soils," *Photogrammetric Eng. Remote Sens.*, vol 40, pp. 87-94, 1974.
- [5] Schott, J.R., Brown, S. D., Raqueno, R. V., Gross, H. N., and Robinson, G., "An Advanced Synthetic Image Generation Model and Its Application to Multi/Hyperspectral Algorithm Development", *Canadian Journal of Remote Sensing*, Vol. 25, No. 2, June 1999.